Probing the electronic properties of the electrified silicon/water interface by combining simulations and experiments

Zifan Ye[a], Aleksander Prominski[b], Bozhi Tian[b], and Giulia Galli[a,b,c,1]

[a]Pritzker School of Molecular Engineering, The University of Chicago, Chicago, IL 60637; [b]Department of Chemistry, The University of Chicago, Chicago, IL 60637; and [c]Materials Science Division, Argonne National Laboratory, Lemont, IL 60439

Contributed by Giulia Galli, October 1, 2021 (sent for review August 12, 2021; reviewed by Ismaila Dabo, Marivi Fernández-Serra, and Ravishankar Sundararaman)

Silicon (Si) is broadly used in electrochemical and photoelectrochemical devices, where the capacitive and Faradaic reactions at the Si/water interfaces are critical for signal transduction or noise generation. However, probing the electrified Si/water interface at the microscopic level remains a challenging task. Here we focus on hydrogenated Si surfaces in contact with water, relevant to transient electronics and photoelectrochemical modulation of biological cells and tissues. We show that by carrying out first-principles molecular dynamics simulations of the Si(100)/water interface in the presence of an electric field we can realistically correlate the computed flat-band potential and tunneling current images at the interface with experimentally measured capacitive and Faradaic currents. Specifically, we validate our simulations in the presence of bias by performing pulsed chronoamperometry measurements on Si wafers in solution. Consistent with prior experiments, our measurements and simulations indicate the presence of voltage-dependent capacitive currents at the interface. We also find that Faradaic currents are weakly dependent on the applied bias, which we relate to surface defects present in newly prepared samples.

electrified interfaces | first-principles molecular dynamics | aqueous interfaces

Silicon-based materials have been used in a myriad of applications, including field-effect-transistor (FET)-based biosensing (1, 2), photoelectrochemical cells for water splitting (3, 4), transient electronics for minimally invasive implants (5), and photodiode-enhanced neuromodulation (6–8) (Fig. 1). In all these devices, the Si surfaces are in contact with water, and the interfaces are either under the effect of an electric field (e.g., in the case of an FET biosensor or a photodiode-enhanced neuromodulator), or undergoing an electrochemical process (e.g., in the case of transient electronics or a water-splitting cell). These Si/water electrified interfaces can produce capacitive and/or Faradaic currents, which in turn can impact the signal transduction mechanism and efficacy of Si-based electrochemical or photoelectrochemical devices. Additionally, unintended electrochemical or photoelectrochemical current leakage at the Si/water interface may raise the noise level of the electronic or optoelectronic devices that are operated in an aqueous environment.

While the understanding and control of electrified semiconductor/water interfaces are important for both fundamental studies and technological applications, experimental approaches that can directly probe the interfacial dynamics and electrochemical reactivity at the atomistic level are still limited (9), especially in transient regimes. The aqueous environment present in biological and electrochemical systems is often rather complex; it includes multiple surface absorbates leading to different charge-transfer mechanisms, and the interplay between the surface chemistry and solvation effects usually hampers a spectroscopic investigation of the electrified electrode/liquid interface at the atomistic level. Computer simulations, on the other hand, can provide valuable information on the structural and electronic properties of aqueous interfaces (10–14) at the atomistic level, especially when first-principles methods (15) are used to describe interatomic forces and bond breaking and formation. When integrated with experiments (16), these simulations may help us understand specific Faradaic and non-Faradaic processes occurring at interfaces that in turn underpin the functions of bioelectronic and electrochemical devices. In Faradaic processes, currents cross the interface by virtue of an electrochemical reaction, while there is no transfer of ions or electrons across the electrode in non-Faradaic (or capacitive) processes. In the latter case, an (equilibrium) charge–voltage (σ-V) curve can be constructed, while in Faradaic processes one can construct a steady-state current–voltage (i-V) curve (17).

Here we focus on processes relevant to transient electronics and photoelectrochemical modulation of biological cells and tissues, where hydrogenated Si surfaces are initially in contact with water. Si-based transient electronics are largely based on the dissolution of Si in water (18), where the Si–H bond attack by water molecules is typically expected to occur. In photoelectrochemical modulation, freshly etched Si nanowires or multilayered membranes are usually prepared and the surface of Si

Significance

Probing electrified interfaces is critical to understanding a myriad of phenomena relevant to transient electronics, photoelectrochemical modulation of biological cells and tissues, and photoelectrocatalysis. However, it remains challenging to devise atomistic models of electrified interfaces that can be used to predict electrochemical processes at the microscopic scale. We present a theoretical study of the hydrogenated silicon/water interface, validated by experiments, and we show that by performing quantum simulations and electronic structure calculations based on first principles one can reliably predict capacitive and Faradaic currents at the electrified interface. Our combined simulation and experimental strategy provide a protocol to understand, at the atomistic level, several properties of Si-based electrochemical or photoelectrochemical devices of interest to transient electronics and biomodulation applications.

Author contributions: G.G. designed research; Z.Y., A.P., and B.T. performed research; Z.Y., A.P., and B.T. analyzed data; and Z.Y., B.T., and G.G. wrote the paper.

Reviewers: I.D., The Pennsylvania State University; M.F.-S., Stony Brook University; and R.S., Rensselaer Polytechnic Institute.

The authors declare no competing interest.

[1]To whom correspondence may be addressed. Email: gagalli@uchicago.edu.

This article contains supporting information online at http://www.pnas.org/lookup/suppl/doi:10.1073/pnas.2114929118/-/DCSupplemental.

Published November 8, 2021.

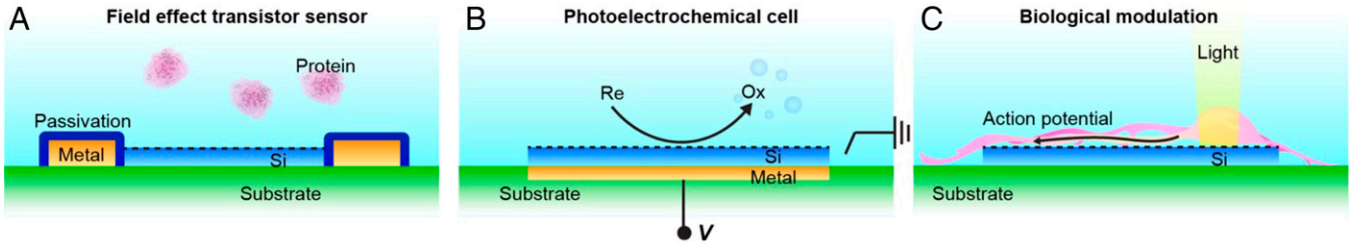

Fig. 1. Electrified Si/water interfaces in silicon-based electronic, electrochemical, and photoelectrochemical devices. The dashed lines denote the Si/water interfaces. (*A*) Si nanowire FET sensor for proteins. The electrified Si/water interface may yield current leakage or corrosion, raising the noise level or causing device failure. (*B*) Si homojunction or heterojunction photoelectrochemical cells. Technically important applications such as water splitting can be assisted by this process. (*C*) Si homojunction- or heterojunction-based biological modulation tool. In one important case, light can produce photoelectrochemical effect at the Si surface for neuromodulation (6).

is hydrogen-terminated (6). To investigate these aqueous interfaces, we generated an atomistic model of the electrified interface between the hydrogenated Si(100) surface and water by performing first-principles molecular dynamics (FPMD) (15) simulations in the presence of an electric field (19, 20). We determined the electronic structure of the interface as a function of the applied bias, including band offsets, flat-band potentials, and interfacial scanning tunneling microscope (STM) images. We then investigated the origin of capacitive and Faradaic processes by directly comparing simulation and experimental results obtained for Si wafers etched in hydrofluoric acid (HF) so as to yield a hydrogen-terminated surface. Our work provides a strategy and a protocol to study electrified interfaces for biological and transient electronic applications, and it gives insight into the atomistic origin of capacitive and Faradaic currents. Interestingly, our simulations, validated by pulsed chronoamperometry measurements, show that capacitive currents depend almost linearly on the magnitude of the applied field, while Faradaic currents are weakly affected by the presence and magnitude of the applied electric field or by doping of the sample.

Results

After equilibrating the H-Si/water interface using FPMD, we computed band offsets and flat-band potentials as a function of the applied field to understand the qualitative behavior of capacitive currents as a function of the applied voltage. The magnitude of the electric field was chosen to be similar to that present when operating Si-based electronic, electrochemical, and photoelectrochemical devices in water (8). Capacitive and Faradaic currents were also measured with the pulsed chronoamperometry method (21, 22) and used to validate our simulation results; in addition, computed STM images were used to characterize and understand the origin of Faradaic processes.

Capacitive Currents. We start by discussing capacitive currents, which originate from an electron accumulation near the solid/water interfacial region, giving rise to an energy barrier at the interface. We investigate such an energy barrier by computing the band offsets between water and the silicon surface and the flat-band potential. The changes of band offsets and flat-band potential as a function of the electric field are indicative of changes in the electron accumulation at the interface, which in turn regulates the presence and magnitude of capacitive currents.

We computed band offsets of several snapshots and averaged the results (*SI Appendix*, Fig. S1), following the protocol of ref. 11. Twenty snapshots, evenly spaced in time, were extracted from an equilibrated MD trajectory, for which we computed the electronic structure at the density functional theory (DFT) level of theory (see *SI Appendix*, Supplementary Note 6 for the discussion of the equilibration process). We then corrected our DFT results for single-particle energy levels using the G_0W_0 approximation (23, 24). Our findings for nonelectrified samples were consistent with previous literature reports (11, 25). The computed position of the valence band maximum (VBM) of Si with respect to vacuum (−5.049 eV) is consistent with the experimental ionization potential 5.29 eV measured for an H-terminated Si(111) surface (26). The band edge positions calculated at the DFT/ Perdew–Burke–Ernzerhof (PBE) (27) level of theory and with G_0W_0 corrections, as a function of the applied field, are summarized in *SI Appendix*, Table S2.

Our results show that the conduction band offset of the electrified samples is decreased with increasing intensity of the applied electric field (Table 1), suggesting a lower energy barrier for electron accumulation at the Si surface or for electron injection into water. To quantify the energy barrier and the effect of the electric field on band bending, we computed the flat-band potentials U_{fb} of the Si surface at the electrochemical interface.

The flat-band potential U_{fb} is defined as the electrochemical potential of an interface at which the semiconductor bands are flat (28). For an n-type semiconductor, which we want to mimic here, it may be expressed with reference to vacuum as

$$U_{fb} = E_{CB} - \Delta E_F + V_{dip} + V_H, \quad [1]$$

where E_{CB} is the position of the conduction band edge and ΔE_F is the energy difference between the Fermi level and the conduction band edge. We determined the position of the Fermi level referenced to vacuum $E_F = E_{CB} - \Delta E_F$ as the midpoint between the conduction band minimum (CBM) and VBM. In Eq. **1** V_{dip} is the potential drop due to the dipole layer formed at the interface (29). The electric field and solvation effect both contribute to determine the values of V_{dip}; since the VBM and CBM were computed in the presence of explicit water molecules, solvation effects are automatically included in our calculations. The contribution from the electric field was obtained from the difference of the electrostatic potential between electrified and nonelectrified samples. The values of E_F and V_{dip} are summarized in *SI Appendix*, Table S3. Finally, V_H is the potential drop across the Helmholtz layer due to ion

Table 1. Computed valence band offsets (VBO), conduction band offsets (CBO), and flat-band potentials (U_{fb}) of the H-Si(100)/water interface as a function of the applied voltage

Voltage, V	VBO, eV	CBO, eV	U_{fb} vs. vacuum, eV	U_{fb} vs. SCE, eV
0	4.01	2.60	−4.37	−0.31
0.35	4.14	2.47	−4.12	−0.56
0.54	4.23	2.38	−3.93	−0.75
0.73	4.38	2.23	−3.64	−1.04

We report results including G_0W_0 corrections on results obtained by carrying out FPMD simulations at the DFT level.

accumulation and absorption at the interface, which in the case of our simulation is zero since we did not include any ions. According to the Nernst equation, at room temperature

$$V_H = 0.059(pH - pH_{PZC}), \quad [2]$$

where pH_{PZC} is the pH value at which the point of zero charge (PZC) condition is realized. By setting V_H to zero, we computed the flat-band potential at PZC conditions; for an Si surface, such a condition corresponds to $pH = pH_{PZC} \sim 2$ to 3 (30). In order to compare with experiments, the computed flat-band potential was referenced to the standard calomel electrode (SCE) on the absolute scale (−4.68 eV) (31). Since the experimental flat-band potential for n-type Si can be sensitive to the exact surface termination and oxidation conditions (32), we compared our computed value with data measured from HF-treated Si samples which are expected to yield hydrogen-terminated surfaces such as those investigated in our simulations. The results, shown in the last two columns of Table 1, indicate that the computed U_{fb} are qualitatively in the range of the experimental U_{fb}, which is around $-0.2 \sim -0.6$ at the PZC (32). We note that the variability of experimental results may be due to measurements carried out in slightly different conditions; for example, the results may depend on the stage of the oxidation process at which the flat-band potential is measured.

Our simulations indicate that for n-type Si in solution the U_{fb} decreases with increasing magnitude of a negative electric field. Such a decrease is expected to lead to a higher degree of electron accumulation at the interface and hence to higher capacitive currents, or to an easier charge injection into water, which would produce Faradaic currents at the electrified n-type Si/water interface. These results are consistent with prior experimental observations, where the photoelectrochemical current produced from a photodiode subject to a larger photovoltage yields stronger amplitude of photocapacitive currents (6).

In order to validate the predictions of our FP simulations and the validity of the model used here, we performed pulsed chronoamperometry experiments (Fig. 2) (21, 22), where negative voltage pulses with different amplitudes were applied to newly prepared n-type Si wafers in an electrochemical setup. We observed that capacitive currents substantially increase with increasing applied voltage intensity (Fig. 2*C*), consistent with the trend observed in our simulations (see Table 1), where the capacitive currents are predicted to increase with the increasing intensity of the electric field. In addition, we found that the Faradaic currents are significantly smaller than the capacitive ones and are weakly dependent on voltage in the high voltage range (Fig. 2*D*).

Faradaic Currents. We turned again to simulations to investigate Faradaic processes at the atomistic level, and to this end we computed STM images of the pristine and electrified H-Si/water interfaces. In the electrochemical measurements, the Faradaic current is associated with surface redox reactions. The change of ion concentrations leads to a charge redistribution in the interfacial region. Such process can be probed by placing a conductive tip near the surface (patch-clamp method), where the ionic flow from the surface to the tip are measured as Faradaic current signals.

The physical processes occurring in STM experiments are similar to those probed by the patch-clamp method (33) used to study Faradaic currents in several devices.

Here, we computed two-dimensional (2D) STM tunneling current images in planes parallel to the interface using the Tersoff–Hamann approximation (34, 35), and we evaluated the local density of states (LDOS):

$$LDOS(\epsilon,x,y) = 2\sum_i |\psi_i(xy)|^2 \delta(\epsilon - \epsilon_i)|_z, \quad [3]$$

where $\psi_i(x,y)$ is the single particle wavefunction projected on a given x–y plane, the factor of 2 accounts for the spin degeneracy, ϵ_i denotes the Kohn–Sham eigenvalues, and z represents the position of the tip above the interface. The tunneling current

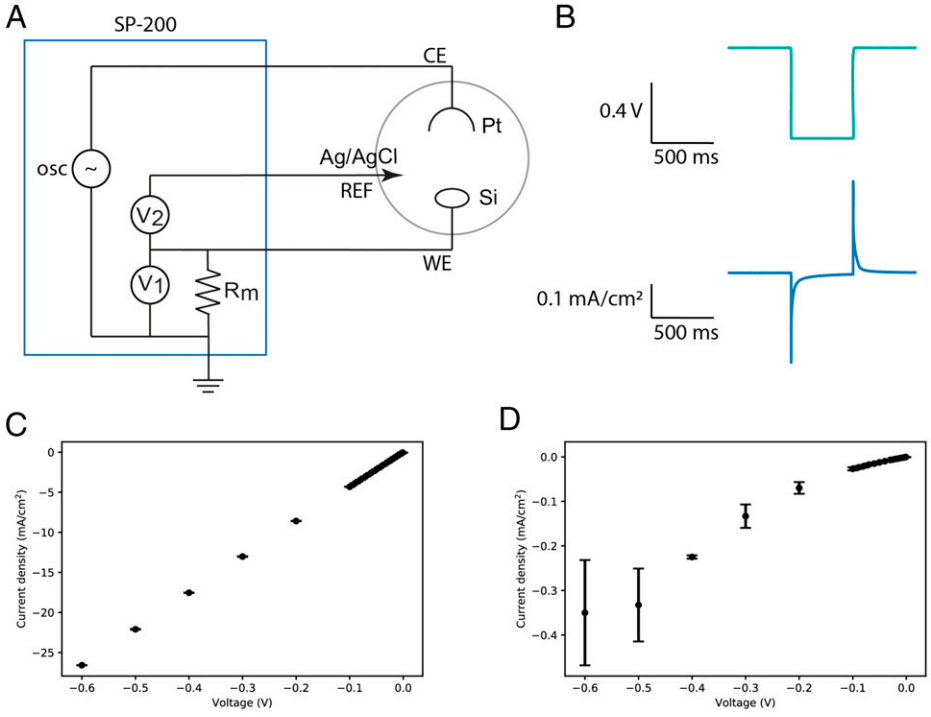

Fig. 2. Pulsed chronoamperometry experiments using silicon electrodes. (*A*) Three-electrode experimental setup used for the measurements. (*B*) Representative voltage traces and recorded current response of the silicon electrode. (*C*) Capacitive current density and (*D*) Faradaic current density as the function of applied voltage. Both the capacitive and Faradaic current of wired Si wafer increases with the increasing of external electric field intensity.

(I) in the x–y plane can then be obtained from the integral of the LDOS:

$$I \propto \int_{\epsilon_f - eV}^{\epsilon_f} LDOS(\epsilon,x,y)d\epsilon, \quad [4]$$

where ϵ_f is the Fermi energy and eV is the bias applied by the tip, which is chosen to be negative to model the electron transfer from the surface to the tip. We first determined the position of the virtual tip by identifying the interfacial region from the LDOS plotted along the direction perpendicular to the interface (36), as shown in Fig. 3. The interfacial region is approximately defined by the two lines parallel to the interface shown in the figure. In our model, we positioned the tip inside the interfacial region, i.e., around 2 Å above the H atoms of the hydrogenated Si(100), thus capturing the current stemming from the interaction between the surface and the interfacial water molecules.

Fig. 4 shows the tunneling current at constant voltage conditions (−200 meV, −700 meV, and −1 eV) obtained from Eq. **4** for the nonelectrified interface. Higher voltage probes energy levels of crystalline structure of Si, as apparent from Fig. 4*C*. Note that increasing the tip bias does not change the position or area of the high-current-density region. We found that the high-current region originates from an interface state (shown in Fig. 5*A*) which is generated by the presence of a dangling bond at the Si surface. Such a defect was introduced manually in our computational sample by removing an H terminating a Si atom and letting it diffuse in the bulk of the water sample. This dangling bond in the computational sample mimics one of the processes which may occur experimentally in the early stages of the oxidization of a freshly prepared H-terminated Si substrate; such a process has been shown to produce hydrogen gas (37, 38).

We note that in our simulation the formation of Si–OH bonds, shown in Fig. 5*B*, can be observed over short time scales, and we expect that such an event would appear multiple times in longer simulations. We also note that the occurrence of this bond was observed in simulations carried out with different density functionals (see *Materials and Methods* and *SI Appendix*, Supplementary Notes 4 and 5) and thus appears to be a robust feature of our computational model.

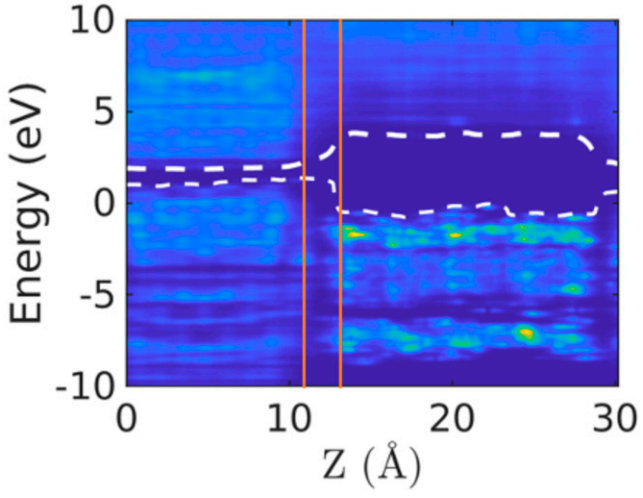

Fig. 3. LDOS projected in the direction perpendicular to the interface (z); the VBM and CBM are indicated by white dashed lines. Note that the LDOS is computed here at the DFT/PBE level for the purpose of identifying an interfacial region, although our computed eigenvalues in Table 1 are all corrected using the G_0W_0 approximation. The interfacial region is shown by the two orange lines.

The oxidation of Si dangling bonds suggests that the Faradaic current might be measurable experimentally only for newly treated surface samples, before the reactive sites are gradually oxidized by water. We note that in the presence of Faradaic currents, devices with aqueous interfaces might degrade over time, consistent with experimental observations in transient electronics and the degradation of Si-based FET sensors.

We also computed the STM images for electrified samples (*SI Appendix*, Fig. S2) and found that the area or position of high-current-density regions showed barely any difference relative to the nonelectrified sample, confirming that the origin of Faradaic currents is related to surface chemistry, on which the influence of the electric field is weak; however, the current density for electrified samples under the tip bias is slightly larger than for the nonelectrified counterpart, consistent with our electronic structure findings.

The results of our calculations showing that the Faradaic processes are weakly dependent on the applied bias are validated by the trends observed in our pulsed chronoamperometry (Fig. 2 *C* and *D*) experiments: While the capacitive currents are linearly proportional to the applied volage, the Faradaic current grows slower in the voltage regime investigated in this study, where presumably not all dangling bond defects present at the surface have been oxidized. This observation also agrees with previous neuromodulation studies, where the intensity of Faradaic currents from Si-based modulators is not significantly enhanced by an increase of the photovoltage (i.e., use of p-i-n diode configuration versus a pure p-type Si) (6).

Discussion

In this work we derived an atomistic model of electrified H-Si/water interfaces from FP to investigate capacitive and Faradaic currents at interfaces and gain insight into the functions of electrochemical devices at the microscopic level. We focused on Si(100), a prototypical semiconducting material, as Si is the most biocompatible and biodegradable of all known semiconductors, and thus relevant to many biological interface studies.

We explicitly devised experiments to validate our models and predictions. In particular, we computed the band offsets at the Si/water interface as a function of the electric field using methods based on DFT (15, 27) and many-body perturbation theory (GW) (23, 24). We then determined the flat-band potentials of a Si electrode (energy barrier) as a function of bias and we found that it decreases when the intensity of the electric field increases, suggesting a high degree of electron accumulation in the case of n-type Si interfaced with water. Such an accumulation may lead to capacitive currents or to injection of charges ultimately responsible for Faradaic currents. The results of our simulations were validated by pulsed chronoamperometry measurements for Si wafers, which consistently showed that capacitive currents depend almost linearly on the magnitude of the applied field. These results are consistent with those of prior studies on the photoelectrochemical currents in Si photodiode-based neuromodulation tools (6).

In addition, we analyzed Faradaic currents by computing 2D tunneling current images corresponding to STM experiments. Similar to the patch-clamp method in photoresponse measurements, STM experiments can probe the current originating from the electrode surface at a given bias and tip position. The tunneling current was obtained by integrating the local density of states (ILDOS) projected on a plane parallel to the surface (34, 35). We found that the high-current-density regions observed in 2D tunneling current images correspond to interface electronic states arising from dangling bonds (defects) present at the Si surface, which we expect to be present in freshly

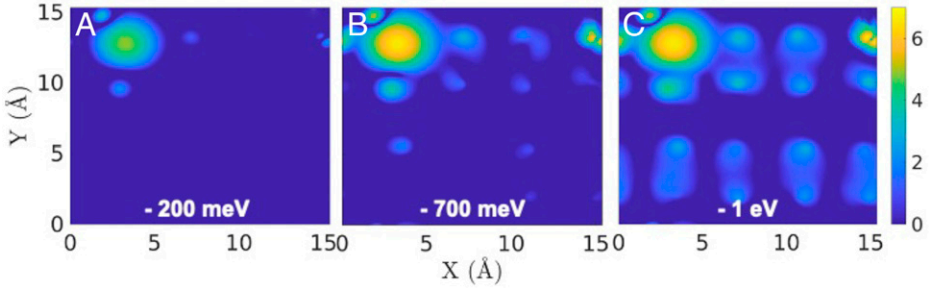

Fig. 4. STM images computed at the interfacial region of the H-Si surface (see Fig. 3) using Eq **4** at (*A*) −200 meV, (*B*) −700 meV, and (*C*) −1 eV. The high current density stemming from the surface reaction corresponds to the brighter region in the images. The color bar is in logarithm scale.

prepared experimental samples. In our simulations we found that the magnitude of Faradaic currents is weakly affected by the presence and magnitude of the applied electric field or by doping, and these results were again confirmed by our patch-clamp experiments (6).

Our combined simulation and experimental study provided a comprehensive picture of the physical properties of the electrified H-Si/water interface and it represents a first, key step in understanding, at the microscopic levels, the Si-based electrochemical or photoelectrochemical devices relevant to transient electronics and biomodulation applications. Interestingly, our findings reveal a previously overlooked origin of Faradaic processes at the Si/water interface. As nanostructured Si has been widely used for a range of applications in solution, the defects of the Si surface (such as dangling bonds or Si–H bonds) may contribute significantly to Faradaic processes that are desirable for several applications, for example in the case of hydrogen evolution at the surface of nanoporous Si particles (39), or in the case of neural modulations with nanocrystalline Si nanowires (7).

Materials and Methods

Computer Simulations and Electronic Structure Calculations. In our simulations we constructed a hydrogenated Si slab to model the electronic properties of Si in contact with water before the formation of the oxidation layer. In order to validate the results of the simulations, in our experiments we etched the Si surfaces with HF to remove any oxidized layers. This treatment yields Si surfaces mostly covered with H atoms, with a small amount of Si dangling bonds due to the corrosion of HF.

In particular, we modeled an H-Si/water interface with a supercell consisting of 124 water molecules interfaced with a eight-layer hydrogenated Si(100) slab with 128 Si atoms, and we terminated the surface with hydrogen atoms. We also introduced a dangling bond on the surface, before equilibration, to mimic the presence of defects that are expected to be present in freshly prepared experimental samples. The interfacial thickness between Si and water was determined using the results of a previous study (11).

We first carried out FPMD using the PBE exchange-correlation functional (27), norm-conserving pseudopotentials (40), and a plane wave basis set and kinetic energy cutoff of 60 Ry. The Γ point was used to sample the Brillouin zone of the supercell. We generated trajectories in the NVT ensemble using the Qbox code (41) at a target temperature of 400 K with the Bussi, Donadio, and Parrinello thermostat (42). The target temperature was chosen to be higher than room temperature to model structural properties of water in better agreement with experiments, when using the PBE functional (43). The whole slab was equilibrated at 400 K, including the Si part (see *SI Appendix* for further discussions). To understand the effect of van der Waals interactions on the description of the properties of liquid water, bulk Si, and the interface we also conducted additional FPMD simulations with the van der Waals density functional optB88 (44) at a target temperature of 330 K. The lattice constants of bulk Si obtained with PBE and opbB88 differ by ∼0.1% (*SI Appendix*, Table S4). We also compared the structural properties of water obtained with optB88 and PBE functionals in the absence of bias. We present a detailed comparison between the results obtained with the two functionals (*SI Appendix*, Figs. S3 and S4); the comparison led us to conclude that for the objectives of this work using the PBE functional is sufficiently accurate and hence we conducted the simulations under bias using PBE.

We performed simulations in the presence of an electric field by carrying out the calculation of the electronic ground state using the electric enthalpy as defined by Souza et al. (20). Hence, at each step of the FPMD we minimized the electric enthalpy functional,

$$\mathcal{F}[u_{nk};\mathbf{E}] = E_{KS} - \Omega \mathbf{P}_{mac}\cdot\mathbf{E}, \qquad [5]$$

where u_{nk} is the periodic part of the field-polarized Bloch function, **E** is the macroscopic field, Ω is the unit cell volume, and E_{KS} is Kohn–Sham energy. The macroscopic polarization $\mathbf{P}_{mac}$ was obtained using the Berry-phase theory (45, 46). The electric field was applied along the direction perpendicular to the surface to model the accumulation of charge that results experimentally when using n-type Si interfaced with water. The field intensities were chosen so that built-in potentials are comparable to those of experimental PIN-Si structures (47), assuming the experimental thickness of the intrinsic layer to be around 150 nm (6). The electric field intensities and built-in potentials used in our work are listed in *SI Appendix*, Table S1. We note that the intensity of the electric field considered here corresponds to energies smaller than thermal energies, and hence the dynamics and structure of water were not perturbed during our FPMD simulations.

We equilibrated and collected FPMD trajectories for pristine and electrified samples for ∼10 and 5 ps, respectively. We checked the equilibration process by monitoring whether the total energy of the system fluctuated at a stable value and whether the system temperatures reached the target. We also calculated the equipartition of energy between different species to verify the equilibration process (*SI Appendix*, Fig. S5).

The data for electronic structure calculations beyond DFT were originally obtained with the WEST code (48) interfaced with Quantum ESPRESSO (48, 49). The latter code was also used for STM image calculations.

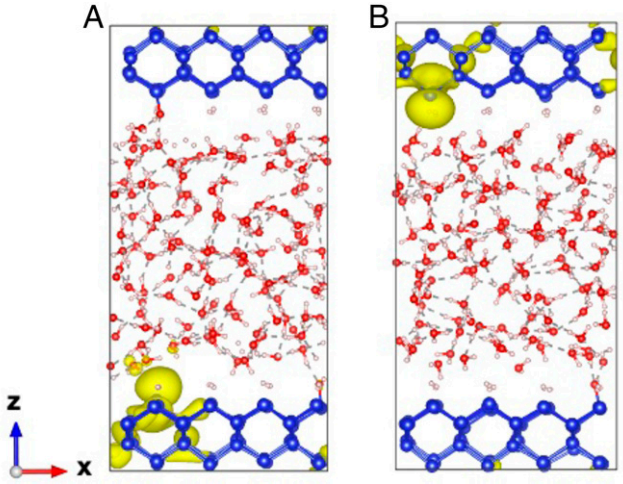

Fig. 5. Iso-surface of the charge density (in yellow) for the states corresponding to a dangling bond at the surface (see main text). Silicon, oxygen, and hydrogen atoms are indicated by blue, red, and white spheres, respectively. *A* and *B* show two configurations of the surface.

Pulsed Chronoamperometry Measurements. In order to measure capacitive and Faradaic currents we performed pulsed chronoamperometry using silicon electrodes. Electrodes were prepared from (100) silicon wafers (550 μm, n-type, 0.001 to 0.005 Ω cm; Nova Electronic Materials). In short, a 5-nm chromium layer and 10-nm gold layer were deposited sequentially on the back side of the 10- × 10-mm wafer using an electron-beam evaporator (EvoVac; Angstrom Engineering). The connecting copper wires were then soldered to the gold contact. The connection, together with part of the front wafer surface, was insulated using a fast-set epoxy (MG Chemicals). The area of tested electrode was ∼0.77 cm^2. Right before the measurement, the electrodes were cleaned in isopropanol in an ultrasonic bath for 5 min. Subsequently, the surface oxide was removed in concentrated HF (48 to 51%; Acros Organics) for 1 min. Finally, the electrode was soaked in ultrapure water for 1 min, washed with copious amounts of ultrapure water, and dried using compressed nitrogen.

Pulsed chronoamperometry was performed using a potentiostat (SP-200; BioLogic) controlled with EC-Lab Express. The time base of measurements was 140 μs. A platinum wire was used as a counterelectrode and an Ag/AgCl (1 M) electrode was used as a reference. For the measurement, the silicon electrode was put into the electrochemical cell filled with phosphate-buffered saline solution at room temperature and had the resting potential of ∼300 mV. A series of 500-ms pulses with variable negative potentials vs. initial electrode resting potential was applied to silver electrode and current transients were measured. The rest period between subsequent pulses was 1,000 ms. Transient currents were taken as a difference between the holding current and the specific points on the response curve: The capacitive current for each pulse was defined as a maximal negative recorded current and the Faradaic current as an average current observed in the last 25 ms of a pulse. The values represent a mean of three recordings from a representative electrode.

Data Availability. Source codes are available at GitLab, Qbox (http://scherzo.ucdavis.edu/qbox/qbox-public) and WEST (http://greatfire.uchicago.edu/west-public/West), and GitHub, Quantum Expresso (https://github.com/QEF/q-e/releases). Data related to this publication are organized using Qresp software (https://qresp.org/), and will be available online at https://paperstack.uchicago.edu/paperdetails/617c303032f83df21c34e5e6?server=https://paperstack.uchicago.edu. All other study data are included in the article and/or *SI Appendix*.

ACKNOWLEDGMENTS. This work was supported as part of the Advanced Materials for Energy-Water Systems Center, an Energy Frontier Research Center funded by the US Department of Energy, Office of Science, Basic Energy Sciences. A.P. acknowledges support from the NSF MRSEC Graduate Fellowship (NSF DMR-2011854). We thank Francois Gygi, Yuanwen Jiang, Han Yang, and Viktor Rozsa for many useful discussions.

1. G. Zheng, X. P. Gao, C. M. Lieber, Frequency domain detection of biomolecules using silicon nanowire biosensors. *Nano Lett.* **10**, 3179–3183 (2010).
2. X. Duan *et al.*, Intracellular recordings of action potentials by an extracellular nanoscale field-effect transistor. *Nat. Nanotechnol.* **7**, 174–179 (2011).
3. S. Y. Reece *et al.*, Wireless solar water splitting using silicon-based semiconductors and earth-abundant catalysts. *Science* **334**, 645–648 (2011).
4. M. G. Walter *et al.*, Solar water splitting cells. *Chem. Rev.* **110**, 6446–6473 (2010).
5. B. Tian *et al.*, Three-dimensional, flexible nanoscale field-effect transistors as localized bioprobes. *Science* **329**, 830–834 (2010).
6. Y. Jiang *et al.*, Rational design of silicon structures for optically controlled multiscale biointerfaces. *Nat. Biomed. Eng.* **2**, 508–521 (2018).
7. R. Parameswaran *et al.*, Photoelectrochemical modulation of neuronal activity with free-standing coaxial silicon nanowires. *Nat. Nanotechnol.* **13**, 260–266 (2018).
8. Y. Jiang, B. Tian, Inorganic semiconductor biointerfaces. *Nat. Rev. Mater.* **3**, 473–490 (2018).
9. M. Favaro *et al.*, Unravelling the electrochemical double layer by direct probing of the solid/liquid interface. *Nat. Commun.* **7**, 12695 (2016).
10. T. A. Pham, Y. Ping, G. Galli, Modelling heterogeneous interfaces for solar water splitting. *Nat. Mater.* **16**, 401–408 (2017).
11. T. A. Pham, D. Lee, E. Schwegler, G. Galli, Interfacial effects on the band edges of functionalized si surfaces in liquid water. *J. Am. Chem. Soc.* **136**, 17071–17077 (2014).
12. C. Zhang, T. Sayer, J. Hutter, M. Sprik, Modelling electrochemical systems with finite field molecular dynamics. *J. Phys. Energy* **2**, 032005 (2020).
13. Z. K. Goldsmith, M. F. Calegari Andrade, A. Selloni, Effects of applied voltage on water at a gold electrode interface from *ab initio* molecular dynamics. *Chem. Sci. (Camb.)* **12**, 5865–5873 (2021).
14. L. S. Pedroza, P. Brandimarte, A. R. Rocha, M.-V. Fernández-Serra, Bias-dependent local structure of water molecules at a metallic interface. *Chem. Sci. (Camb.)* **9**, 62–69 (2017).
15. R. Car, M. Parrinello, Unified approach for molecular dynamics and density-functional theory. *Phys. Rev. Lett.* **55**, 2471–2474 (1985).
16. C.-Y. Li *et al.*, In situ probing electrified interfacial water structures at atomically flat surfaces. *Nat. Mater.* **18**, 697–701 (2019).
17. P. Biesheuvel, S. Porada, J. Dykstra, The difference between Faradaic and non-Faradaic electrode processes. arXiv [Preprint] (2018). https://arxiv.org/abs/1809.02930 (Accessed 26 September 2021).
18. J. A. Rogers, T. Someya, Y. Huang, Materials and mechanics for stretchable electronics. *Science* **327**, 1603–1607 (2010).
19. H. Zheng, M. Govoni, G. Galli, Dielectric-dependent hybrid functionals for heterogeneous materials. *Phys. Rev. Mater.* **3**, 073803 (2019).
20. I. Souza, J. Iñiguez, D. Vanderbilt, First-principles approach to insulators in finite electric fields. *Phys. Rev. Lett.* **89**, 117602 (2002).
21. A. J. Bard, L. R. Faulkner, Fundamentals and applications. *Electrochemical Methods* **2**, 580–632 (2001).
22. A. Molina, J. González, *Pulse Voltammetry in Physical Electrochemistry and Electroanalysis* (Monographs in Electrochemistry, Springer, 2016).
23. M. S. Hybertsen, S. G. Louie, First-principles theory of quasiparticles: Calculation of band gaps in semiconductors and insulators. *Phys. Rev. Lett.* **55**, 1418–1421 (1985).
24. L. Hedin, New method for calculating the one-particle Green's function with application to the electron-gas problem. *Phys. Rev.* **139**, A796 (1965).
25. T. Anh Pham *et al.*, Band offsets and dielectric properties of the amorphous Si3N4/Si (100) interface: A first-principles study. *Appl. Phys. Lett.* **102**, 241603 (2013).
26. R. Hunger *et al.*, Chemical and electronic characterization of methyl-terminated Si (111) surfaces by high-resolution synchrotron photoelectron spectroscopy. *Phys. Rev. B* **72**, 045317 (2005).
27. J. P. Perdew, K. Burke, M. Ernzerhof, Generalized gradient approximation made simple. *Phys. Rev. Lett.* **77**, 3865–3868 (1996).
28. M. Gerosa, F. Gygi, M. Govoni, G. Galli, The role of defects and excess surface charges at finite temperature for optimizing oxide photoabsorbers. *Nat. Mater.* **17**, 1122–1127 (2018).
29. Y. Ping, R. Sundararaman, W. A. Goddard III, Solvation effects on the band edge positions of photocatalysts from first principles. *Phys. Chem. Chem. Phys.* **17**, 30499–30509 (2015).
30. J.-P. Cloarec *et al.*, pH driven addressing of silicon nanowires onto Si3N4/SiO2 micropatterned surfaces. *Nanotechnology* **27**, 295602 (2016).
31. S. Trasatti, The absolute electrode potential: An explanatory note (recommendations 1986). *Pure Appl. Chem.* **58**, 955–966 (1986).
32. S. Ottow, G. Popkirov, H. Föll, Determination of flat-band potentials of silicon electrodes in HF by means of ac resistance measurements. *J. Electroanal. Chem. (Lausanne)* **455**, 29–37 (1998).
33. Y. Jiang *et al.*, Nongenetic optical neuromodulation with silicon-based materials. *Nat. Protoc.* **14**, 1339–1376 (2019).
34. J. Tersoff, D. Hamann, Theory and application for the scanning tunneling microscope. *Phys. Rev. Lett.* **50**, 1998 (1983).
35. J. Tersoff, D. R. Hamann, Theory of the scanning tunneling microscope. *Phys. Rev. B Condens. Matter* **31**, 805–813 (1985).
36. H. Yang, M. Govoni, G. Galli, Improving the efficiency of G_0W_0 calculations with approximate spectral decompositions of dielectric matrices. *J. Chem. Phys.* **151**, 224102 (2019).
37. W. S. Liao, S. C. Lee, Water-induced room-temperature oxidation of Si–H and Si–Si bonds in silicon oxide. *J. Appl. Phys.* **80**, 1171–1176 (1996).
38. D. Liu *et al.*, The nature of photocatalytic "water splitting" on silicon nanowires. *Angew. Chem. Int. Ed. Engl.* **54**, 2980–2985 (2015).
39. F. Dai *et al.*, Bottom-up synthesis of high surface area mesoporous crystalline silicon and evaluation of its hydrogen evolution performance. *Nat. Commun.* **5**, 3605 (2014).
40. D. Hamann, M. Schlüter, C. Chiang, Norm-conserving pseudopotentials. *Phys. Rev. Lett.* **43**, 1494 (1979).
41. F. Gygi, Architecture of Qbox: A scalable first-principles molecular dynamics code. *IBM J. Res. Develop.* **52**, 137–144 (2008).
42. G. Bussi, D. Donadio, M. Parrinello, Canonical sampling through velocity rescaling. *J. Chem. Phys.* **126**, 014101 (2007).
43. W. Dawson, F. Gygi, Equilibration and analysis of first-principles molecular dynamics simulations of water. *J. Chem. Phys.* **148**, 124501 (2018).
44. J. Klimeš, D. R. Bowler, A. Michaelides, Chemical accuracy for the van der Waals density functional. *J. Phys. Condens. Matter* **22**, 022201 (2010).
45. R. D. King-Smith, D. Vanderbilt, Theory of polarization of crystalline solids. *Phys. Rev. B Condens. Matter* **47**, 1651–1654 (1993).
46. D. Vanderbilt, R. D. King-Smith, Electric polarization as a bulk quantity and its relation to surface charge. *Phys. Rev. B Condens. Matter* **48**, 4442–4455 (1993).
47. S. M. Sze, Y. Li, K. K. Ng, *Physics of Semiconductor Devices* (John Wiley & Sons, 2021).
48. M. Govoni, G. Galli, Large scale GW calculations. *J. Chem. Theory Comput.* **11**, 2680–2696 (2015).
49. P. Giannozzi *et al.*, QUANTUM ESPRESSO: A modular and open-source software project for quantum simulations of materials. *J. Phys. Condens. Matter* **21**, 395502 (2009).